BIBECHANA
Vol. 21, No. 1, April 2024, 12–22

ISSN 2091-0762 (Print), 2382-5340 (Online)
Journal homepage: http://nepjol.info/index.php/BIBECHANA
Publisher: Dept. of Phys., Mahendra Morang A. M. Campus (Tribhuvan University)Biratnagar

Lattice thermal conductivity in half-Heusler Model compounds XNiSn (X=Ti, Zr, Hf) using Slack's model

Prakash Khatri[1,2], **N. P. Adhikari**[1,*]

[1] *Central Department of Physics, Institute of Science and Technology, Tribhuvan University, Kirtipur, Kathmandu, Nepal*
[2] *Department of Physics, Siddhanath Science Campus, Mahendranagar, Tribhuvan University, Nepal*

[*]Corresponding author. Email: narayan.adhikari@cdp.tu.edu.np

Abstract

Reducing lattice thermal conductivity (κ_l) that reflects the material's heat-carrying capacity through lattice phonon vibrations is crucial for optimizing the figure of merit (zT). Using density functional theory (DFT) and density functional perturbation theory (DFPT), present work considers the structural, electronic, magnetic, and phonon properties of the XNiSn (X=Ti, Zr, Hf) half Heusler (hH) compounds. TiNiSn, ZrNiSn, and HfNiSn are identified as semiconductors with indirect band gaps of 0.43 eV, 0.47 eV and 0.39 eV, respectively, exhibiting dynamical stability. The temperature- dependent κ_l of hH XNiSn are compared using Slack's model with two approaches for analyzing phonon velocity: elastic constants from quasi-harmonic approximation (QHA) as implemented in the Thermo_pw code and slope of phonon bands based on DFPT. At room temperature, TiNiSn, ZrNiSn and HfNiSn have κ_l values of 28.61 $Wm^{-1}K^{-1}$, 34.61 $Wm^{-1}K^{-1}$ and 29.85 $Wm^{-1}K^{-1}$ respectively using phonon velocity from slopes of phonon bands based on DFPT. These values show deviation of 1.48%, 6.29%, and 5.82% to those κ_l values 29.01 $Wm^{-1}K^{-1}$', 36.79 $Wm^{-1}K^{-1}$ and 31.59 $Wm^{-1}K^{-1}$ for TiNiSn, ZrNiSn and HfNiSn respectively using QHA.

Keywords
Density functional theory, Lattice thermal conductivity, Slack's model, Phonon bands.

Article information
Manuscript received: September 16, 2023; Revised: December 5, 2023; Accepted: December 16, 2023
DOI https://doi.org/10.3126/bibechana.v21i1.58405

1 Introduction

The rising energy demands but limited fossil fuels have led to a worldwide energy crisis. Waste heat resulting from industrial processes, residential heating and vehicle exhaust affects the environment. The potential of thermoelectric (TE) materials to utilize such waste heat energy can play a vital role on the reduction of fossil fuel usage and global greenhouse emissions [1–3]. The thermoelectric figure of merit (zT) is employed as a means to quantify the conversion efficiency of thermoelectric materials. It is expressed as [4],

$$zT = \frac{s^2 \sigma T}{\kappa} \tag{1}$$

It depends on the material's transport coefficients, including the Seebeck coefficient (S), electrical conductivity(σ), absolute temperature (T) and total thermal conductivity $\kappa = \kappa_{ele} + \kappa_l$, which is the sum of electronic component (κ_{ele}) and lattice component of total thermal conductivity (κ_l). Thermal conductivity (κ) is crucial for various technological advancements, including thermoelectricity and heat management applications [5,6]. The transport coefficients S, σ and κ_{ele} are interdependent due to the influence of carrier concentration and effective mass. The interdependence between the K_{ele} and σ is established by the Wiedemann-Franz law ($\kappa_{ele} = \sigma$LT). A zT in TE materials corresponds to a high power factor (PF = $S^2\sigma$) and a low κ_l. Strong electron-phonon coupling in bulk materials like half-Heusler (hH) alloys imposes restrictions on simultaneous optimization of PF and reduction of K [7,8].

Nowadays the primary focus is on reducing κ_l since efforts to manipulate κ_{ele} are ineffective due to its direct correlation with σ. It is worth noting that the reduction of κ_l has shown limited impact on the PF. As a result, reducing κ_l independently of the parameters S, σ , and κ_{ele} becomes crucial in optimizing zT value [9]. The lattice thermal conductivity of solid [10], $\kappa_l = 1/3 C_v v_s l$, is directly influenced by the phonon velocity (v_s) and mean free path (MFP) (l). By increasing the scattering of phonons, the heat flux can be reduced hindering MFP and resulting in lower κ_l [11]. Multiple methods like grain boundary scatterings, point defects, dislocations, impurity scattering [12], nanostructuring [13], alloy scattering [14] leading anharmonicity reduce κ_l by scattering phonons. The dominant scattering mechanism in a material is temperature dependent. At low temperatures, grain boundary scattering are significant whereas near to Debye temperature, defects act as scattering centers and above room temperature phonon-phonon scattering dominates [15, 16]. Phonon Boltzmann transport equation (PBTE) [17] involving large numbers of linear equations are challenging to solve for κ_l due to high dimensionality and complexity of determining reliable II and III-order force constants based on atomic interactions [18]. Iterative solutions based on DFT calculations, such as ShengBTE software [19], temperature gradient molecular dynamics (MD) simulations based software tools like LAMMPS [20] require a high computational cost [20]. The Debye-Callaway model offers a method to estimate κ_l using Debye temperature (θ_D), phonon velocity (v_s), and the Grüneisen parameter (Υ) [21]. Slack developed a model [22] (Equation 3) to express the κ_l in semiconductors, considering the significant role of acoustic modes in heat transfer.

Half-Heusler compounds display a wide range of thermal conductivities [7]. The presence of symmetry in hHs contributes to a decreased computational cost in comparison to more intricate systems like layered compounds or those with distorted symmetries [23]. The κ_l of the 18 valence electron system XNiSn (X=Ti, Zr, Hf) has been reported in many experimental and computational studies [8, 24–28]. Instead of computationally expensive models, the Slack model is more efficient and feasible to predict the lattice thermal conductivity (κ_l) and providing insights into thermal transport. To our best knowledge, a comprehensive comparison of the κ_l values for these compounds using Slack's model is still not available. Such a comparison could be beneficial in the field of high-throughput computations to seek for the materials with ultralow or ultrahigh κ_l efficiently. It could eliminate the need for extensive efforts in calculating the Debye temperature and Grüneisen parameter, as required by alternative methods. In the present work, our primary focus is on calculating κ_l of hH XNiSn (X=Ti, Zr, Hf) using Slack's equation. We obtained the required parameters for the equation from two different approaches: from elastic constants by QHA in thermo_pw code [29] implemented in Quantum ESPRESSO and the slopes of acoustical branches of phonon bands using DFPT [30].

The paper is structured as follows: second section discusses the computational details, the third section focuses on the main results and discussion and the last section presents the conclusions and concluding remarks of present work.

2 Computational Details

We used DFT [31] in Quantum ESPRESSO (version 7.1) [32] with a plane wave basis set and generalized gradient approximation (GGA) method with Perdew, Burke and Ernzerhof (PBE) exchange-correlation functional [33]. The RRJK model [34] of ultrasoft pseudopotentials was used for calculations on structural optimization, electronic and magnetic properties. We incorporated a ki-

netic energy cutoff of 70 Ry and a charge density cutoff of 700 Ry with Brillouin zone integration utilized the Monkhorst–Pack scheme [35] with a 10 × 10 × 10 k-mesh in the first irreducible Brillouin zone. The "david" diagonalization method with a mixing factor of 0.3 is employed in the self-consistent field (SCF) calculations, with a convergence threshold of 10^{-6} Ry. For band structure calculations, k-points were chosen along Γ→X→W→K→Γ→L→U→W→L→K, high symmetry path (Figure 1(c)), in the first Brillouin zone of reciprocal lattice. The density of states and partial density of states were computed through non-self consistent field (nscf) calculations with a denser mesh of 20 × 20 × 20 k-points. Marzarri-Vanderbilt smearing [36] of broadening width of 0.005 Ry was employed in all calculations. The compounds' dynamical stability was checked via phonon dispersion calculations using density functional perturbation theory (DFPT) with a 2 × 2 × 2 q-point mesh by computing second-order derivative of the total energy with respect to atomic displacements. The Slack's equation was used for calculating κ_l with velocity of phonon determined using two different techniques. The first method involved the utilization the elastic parameters obtained from QHA implemented in thermo_pw codes. On the other hand, the second approach employed the slopes of the longitudinal and transverse components of the acoustic branches in the phonon dispersion curve.

3 Results and Discussion

3.1 Structural Properties

The XNiSn (X=Ti, Zr, Hf) half-Heusler compounds are extensively studied ternary intermetallics,having an edge-centered cubic structure with a fundamental composition of 1:1:1. The structure has the specific symmetry of F $\bar{4}$ 3m with X element is the most electropositive. Inside the unit cell of these compounds, three atoms (X, Ni, and Sn) are situated at specific in-equivalent Wyckoff positions: X at 4a (0, 0, 0), Ni at 4b (0.5, 0.5, 0.5), and Sn at 4c (0.25, 0.25, 0.25) as shown in figure 1(a) and 1(b).

We have calculated the optimized lattice parameters of XNiSn (X=Ti, Zr, Hf) by minimizing total energy of crystal with Murnaghan's equation of state [37],

$$E(V) = E_0 + \frac{BV}{B'}\left[\frac{1}{B'-1}\left(\frac{V_0}{V}\right)^{B'} + 1\right] \quad (2)$$

In the equation B is bulk modulus, B' is first pressure derivative of the bulk modulus that corresponds to pressure of P=0, E_0 is the equilibrium energy and V_0 is the unit-cell volume that corresponds to zero pressure.

The optimized lattice constant represents the minimum ground state energy, signifying the crystal's most stable configuration. Figure 2(a), 2(b) and 2(c) shows the total energy vs lattice parameter for TiNiSn, ZrNiSn and HfNiSn respectively. The optimized lattice constant for TiNiSn, ZrNiSn and HfNiSn are 11.259 Bohr (5.958Å), 11.629 Bohr (6.154Å) and 11.552 Bohr (6.113Å) respectively. The HfNiSn compound exhibits smaller lattice parameters compared to ZrNiSn and this difference can be attributed to the lanthanide contraction phenomenon. Table 1. presents the optimized lattice constants for XNiSn (X= Ti, Zr, and Hf) along with the previously reported experimental and computational data. The deviation of our calculated lattice parameter values from that in experimental reports by Aliev et al. [38] are 0.63%, 0.71% and 0.76% for TiNiSn, ZrNiSn and HfNiSn respectively. The calculated lattice parameter values in the present work agree with the values in computational report by Öğüt, S., Rabe [39] within 1.36%-2.66%, J. Yang et al. [40] within 0.47%-0.66% and Muta et al. [26] within 0.47%-0.71%. All the variation in lattice parameters are ≤ 2.66% and the variation could be attributed due to the choice of exchange-correlation functional utilized in the studies.

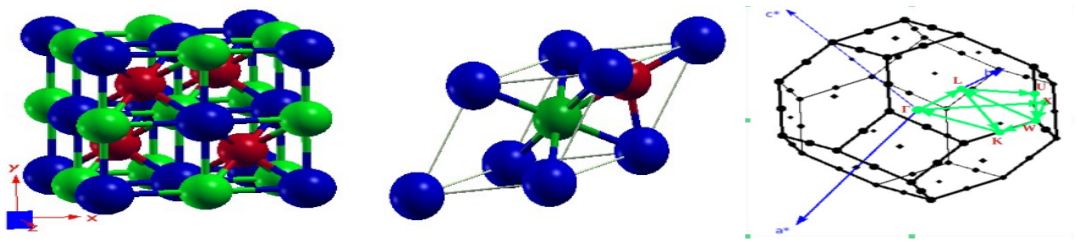

Figure 1: (a) Conventional unit cell of XNiSn (X=Ti, Zr, Hf), (b) Primitive unit cell of XNiSn (X=Ti, Zr, Hf). The blue, red, and green colors in both figures represent X, Ni, and Sn, respectively visualized by XcrySDen. (c) Brillouin zone locating symmetric points.

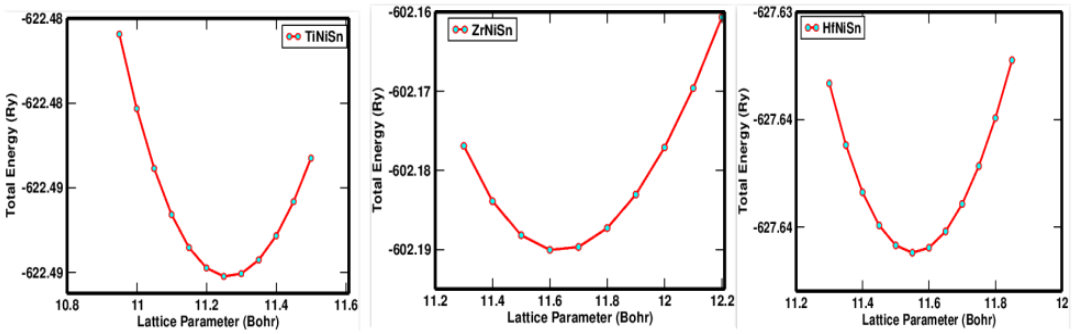

(a) (b) (c)

Figure 2: Total energy (in Rydberg) VS lattice parameter (in Bohr) for (a) TiNiSn (b) ZrNiSn (c) HfNiSn.

Table 1: Comparison of calculated lattice parameter (in Å) of XNiSn (X=Ti, Zr, Hf) with experimental and computational results in literature.

Compound	**Our Work**	**Aliev et al.[38]**	**Öğüt, S., & Rabe[39]**	**J. Yang et al.[40]**	**Muta et al.[26]**
TiNiSn	5.958	5.920	5.814	5.921	5.930
ZrNiSn	6.154	6.110	6.070	6.113	6.110
HfNiSn	6.113	6.066	5.950	6.084	6.080

3.2 Electronic and Magnetic Properties

We have studied the band structures of XNiSn (X=Ti, Zr, Hf) using GGA-PBE exchange-correlation functional as shown in figures 3(a), 3(b) and 3(c). From computed band structure of XNiSn compounds, all the compounds exhibit a semiconductor nature with an indirect band gap. The position of the conduction band minimum (CBM) is at the X point of the Brillouin zone (BZ), while the valence band maximum (VBM) is at the Γ point of the BZ. The TiNiSn, ZrNiSn, and HfNiSn compounds exhibit band gaps (E_g) of 0.43 eV, 0.47 eV, and 0.39 eV, respectively. The calculated band gap values agree with the values in computational report by Öğüt, S., & Rabe [39] within 8.51%-23.07%, J. Yang et al. [40] within 0.00%-8.51% and Zou et al. [41] within 7.69%-10.64% as shown in Table 2. These deviations might be because of the different exchange correlation functional used in the calculations in different studies. In general, DFT underestimates the band gaps. However, in these compounds, the experimental band gap value reported in Aliev et al. [38] is smaller than the calculated value. This difference is because of the formation of an impurity band within the gap, which occurs due to the presence of Ni-interstitial atoms [42].

Density of states (DoS) and partial density of states (PDoS) plots revealing the distribution of electrons among atomic orbitals are crucial tools for understanding the electronic and magnetic properties of materials. The main contribution to the DoS of XNiSn near the Fermi level arises from the 3d orbitals of Ni in the valence band (VB), while it comes from the 3d/4d/5d orbitals of Ti, Zr,and Hf, respectively in the conduction band (CB). The Sn-5p orbitals play a minor role in both the VB and CB of the material. Symmetric and equal electron spin distribution in mentioned orbitals cancels magnetic moments, that explains the non-magnetic behavior in XNiSn compounds. The non-magnetic behavior in these 18 VEC hH is in agreement with the Slater-Pauling rule [43], which connects the material's magnetic moment (M) to the number of valence electrons (Z) in the unit cell as M= (Z-18)μ_B.

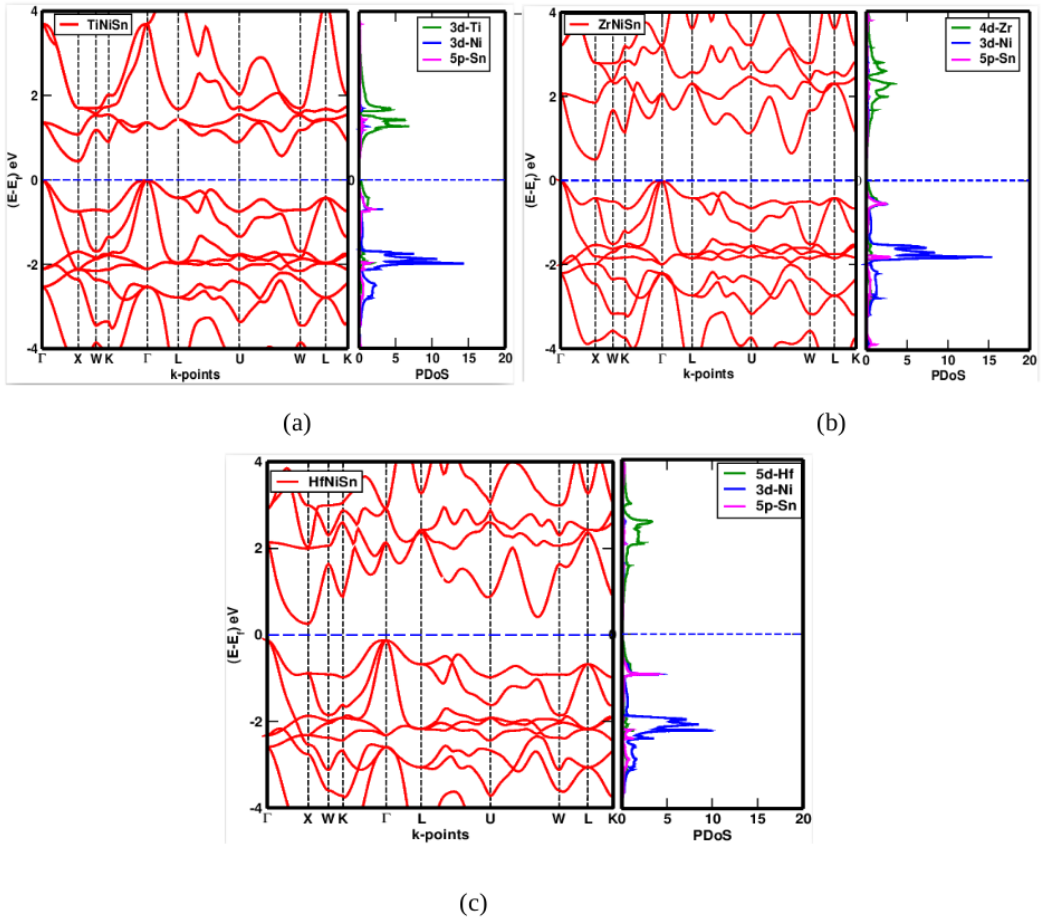

Figure 3: The electronic band structure and PDoS plots of orbitals of constituent atoms (a) TiNiSn (b) ZrNiSn (c) HfNiSn with the Fermi level represented by a horizontal dotted line.

Table 2: Comparison of band gap (E_g in eV) of XNiSn (X=Ti, Zr, Hf) with experimental and theoretical results reported in literatures.

Compound	**Our Work**	**Aliev et al.[38]**	**Öğüt, S., & Rabe[39]**	**J. Yang et al.[40]**	**Zou et al.[41]**
TiNiSn	0.43	0.12	0.51	0.45	...
ZrNiSn	0.47	0.18	0.51	0.51	0.52
HfNiSn	0.39	0.22	0.48	0.39	0.36

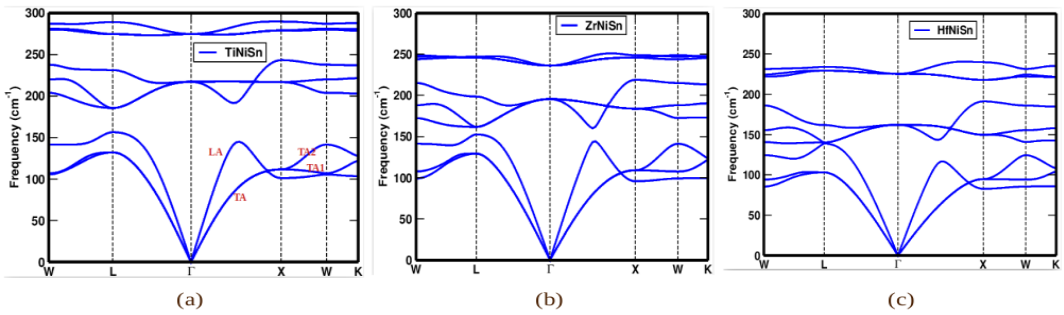

Figure 4: Phonon band diagram of (a) TiNiSn, (b) ZrNiSn and (c) HfNiSn compounds.

3.3 Phonon Spectrum and dynamical stability

This study presents the phonon dispersion of XNiSn (X=Ti, Zr, Hf) using DFPT as shown in figures 4(a), 4(b) and 4(c) respectively. The compounds were checked for dynamical stability using these curves. Stability is indicated by real frequencies, while instability is indicated by imaginary frequencies. Figure 4's phonon dispersion curves confirms the dynamic stability of the compounds, as they lack imaginary phonon frequencies. With a primitive unit cell having 3 atoms, these compounds have three low-frequency acoustic modes and six high-frequency optical modes in their phonon dispersion curve. The equation $v_g = \frac{d\omega}{dk}$ defines phonon group velocity, where optical dk branches exhibit a low group velocity due to their flat curvature, while acoustic branches show a high group velocity with a linear variation. Thus, the acoustic modes play a significant role in heat transport and κ_l, while the optical branch has a minor impact. There is a noticeable separation between the optical and acoustic phonon modes, which decreases from TiNiSn to HfNiSn. The low κ_l might be achieved in the compounds having a small phonon gap or maximum overlapping because of enhanced phonon scattering [44]. The overlapping of phonon modes increases in the order of Ti < Zr < Hf, consequently strongly influencing the thermal transport of phonons in the same order. The maximum acoustic mode frequency for TiNiSn (156 cm^{-1}), ZrNiSn (153 cm^{-1}) and HfNiSn (140 cm^{-1}). The low-energy acoustic phonons have limited energy transfer during heat transport, which ultimately leads to a low κ_l in these materials. Among these compounds, the low frequency for acoustic modes in the phonon is least for HfNiSn.

3.4 Estimation of lattice thermal conductivity

Slack's equation [22] for calculating κ_l is,

$$\kappa_l = \frac{V^{1/3} A M \theta_D^3}{\gamma^2 T n^{2/3}} \tag{3}$$

The parameters in the equation are average atomic mass (M), volume per cell (V), number of atoms in the primitive unit cell (n), Grüneisen parameter (γ) and Debye temperature (θ_D). The Grüneisen parameter (γ) is a measure of the strength of lattice anharmonicity in a material that influences κ_l. It can be determined by considering the longitudinal (v_l) and transverse (v_t) velocities of the lattice vibrations. Our calculations are focused on determining the γ through the analysis of elastic constants [45].

Grüneisen parameter (γ) is computed as,

$$\gamma = \frac{9 - 12(v_t/v_l)^2}{2 + 4(v_t/v_l)^2} \tag{4}$$

The dimensionless constant A is computed as

$$A = \frac{2.43 \times 10^{-8}}{1 - 0.514/\gamma + 0.228/\gamma^2} \tag{5}$$

The v_l and v_t were calculated using two different techniques. The first method used the elastic parameters obtained from QHA implemented in thermo_pw codes. The thermo_pw algorithm calculates the various elastic constants and utilized them to derive various elastic properties, including bulk moduli, shear moduli and Young's moduli, using the Voigt-Reuss-Hill approximation [46, 47]. These derived elastic properties were then employed to compute sound velocities.

$$B = \frac{C_{11} + 2C_{12}}{3} \tag{6}$$

$$G = \frac{\frac{C_{11} - C_{12} + C_{13}}{5} + \frac{5(C_{11} - C_{12})}{3(C_{11} - C_{12} + 4C_{44})}}{2} \tag{7}$$

$$Y = \frac{9BG}{3B + G} \tag{8}$$

The longitudinal and transverse velocity components of lattice vibration are,

$$v_t = \sqrt{\frac{G}{\rho}} \tag{9}$$

$$v_l = \sqrt{\frac{3B + 4G}{3\rho}} \tag{10}$$

The average sound velocity,

$$v = \left[\frac{1}{3}\left(\frac{1}{v_l^3} + \frac{2}{v_t^3}\right)\right]^{-1/3} \tag{11}$$

Another significant factor in computing κ_l is the Debye temperature θ_D, which considers the average sound velocities. The θ_D corresponds to the state where all phonon modes in a material are fully excited and it plays a crucial role in γ and hence κ_l [47]. θ_D determined form the average sound velocities of acoustic phonon modes [46],

$$\theta_D = \frac{\hbar}{k_B}\left(\frac{6\pi^2 n}{V}\right)^2 \nu \tag{12}$$

The second method involves the calculation of the v_l and v_t by analyzing the slopes of longitudinal and transverse components of the acoustic branches respectively in the phonon dispersion curves depicted in Figure 4(a), 4(b) and 4(c). When computing κ_l, the linear region near the Γ point in the acoustic branch of the phonon dispersion curve is selected

because it impacts the thermal transport significantly. The region is selected with care to ensure linearity.

Table 3. presents the v_l , v_t, v, θ_D, γ and κ_l (at 300K) of XNiSn compounds. The κ_l of determined using velocity values from phonon slopes by DFPT and QHA model in thermo_pw codes, are TiNiSn (28.61 $Wm^{-1}K^{-1}$ and 29.00 $Wm^{-1}K^{-1}$), ZrNiSn (34.61 $Wm^{-1}K^{-1}$ and 36.79 $Wm^{-1}K^{-1}$) and HfNiSn(29.85 $Wm^{-1}K^{-1}$ and 31.59 $Wm^{-1}K^{-1}$) respectively. The results obtained from both methods show an agreement of 1.48%, 6.29%, and 5.82% for TiNiSn, ZrNiSn, and HfNiSn, respectively. The variation of κ_l calculated using both approaches for all compounds are as shown in Figure 5. Both approaches calculate κ_l from elastic parameters but differ in the way of estimation. These approaches have varying accuracy in velocity estimations. For phonon velocity from phonon band slopes, the acoustic branches near the point in a specific and localized region of the phonon dispersion curve are analyzed. The another approach estimates the phonon velocities by calculatingthe macroscopic elastic parameters from elastic constants without explicitly considering individual phonon vibrational modes.

Figure 5. demonstrates the temperature-dependent nature of κ_l. Our data shows the trend κ_l (TiNiSn) $<$ κ_l (HfNiSn) $<$ κ_l (ZrNiSn) throughout the considered temperature range. As the temperature increases, the κ_l decreases and becomes less temperature dependent at higher temperatures. This is because of the increased lattice scattering due to increased anharmonicity. The greatest difference between values of κ_l from both approaches at room temperatures is for TiNiSn and ZrNiSn. The deviation in values of κ_l between TiNiSn and ZrNiSn is by 20.97% and 26.81% from the phonon band slope of DFPT and QHA model respectively. On increasing temperature the deviation in the values of κ_l decreases. Despite having high κ_l at room temperature, these compounds exhibit low κ_l at elevated temperatures, making them suitable for high-temperature TE applications and can have better zT values.

Our calculated values by both approach are compared to those reported in Quinn et al.[3] (Ref. [3])in table 3. The calculated values of κ_l in present work by DFPT approach agree within (1.36%-8.06%) and values by QHA model agree within (0.13%-1.65%) to those values reported in Ref. [3].

The κ_l values reported in Ref. [3] used Debye Callaway's model considering Umklapp scattering only. However, if grain boundaries, point defects, and electron-phonon interactions were accounted, κ_l values would be much lower. PHONO3PY, solving Boltzmann transport equation using the relaxation-time approximation (RTA-BTE), reports κ_l values $<$ 10 $Wm^{-1}K^{-1}$ for these compounds by considering anharmonicity resulting from phonon-phonon scattering, mass disorder and grain boundary effects [48, 49]. The values κ_l are 14.5, 16.7 and 15.3 $Wm^{-1}K^{-1}$ calculated by RTA-PBE approach [24], 17, 18, 19 $Wm^{-1}K^{-1}$ by DFT and machine learning [23] and 16.8, 17.5 and 19.5 $Wm^{-1}K^{-1}$ by machine learning algorithm [25] for TiNiSn, ZrNiSn and HfNiSn respectively are lesser κ_l than our calculated values. Although our data agrees the trend with these literature but are highly overestimated. Slack's model shows a similar tendency to overestimate κ_l values in comparison to ShengBTE for NbFeSb and TaFeSb. The κ_l for NbFeSb and TaFeSb at room temperature, as estimated by ShengBTE, are approximately 22 and 21 $Wm^{-1}K^{-1}$, while those predicted by Slack's model are higher at 24 and 26 $Wm^{-1}K^{-1}$, respectively [45]. Slack's model predicts higher κ_l values (12.69, 18.26, and 20.83) $Wm^{-1}K^{-1}$ for MCoBi (M = Ti, Zr, and Hf) in Ref. [50] compared to the values (11.02, 11.14, and 10.43) $Wm^{-1}K^{-1}$ in Ref. [51]. Slack's method offers the main advantage of being computationally intensive, but gives only a rough estimate and lacks accuracy for κ_l. The main drawback is that κ_l is indirectly derived from either elastic constants or acoustic phonons [45, 49]. Despite having limited heat transfer capabilities, modes related to the optical branch can influence κ_l by interacting with acoustic vibrations. Slack's method efficiently predicts both extremely low and high κ_l for compounds in high-throughput computations, particularly in the identification of potential thermoelectric materials. The experimental κ_l values are significantly lower because even if the impurity concentrations are very low, the presence of small amounts of interstitial can cause significant disorder, leading to a substantial reduction in κ_l [2, 26]. In order to achieve closer agreement between computational results and experimental values for κ_l, the consideration of phonon scattering is essential.

Table 3: Comparison of physical properties of XNiSn (X=Ti, Zr, Hf) computed using phonon band slopes in DFPT and QHA in `thermo_pw` codes, along with a comparison to Ref.[3] that reported κ_l values for defect-free compositions based on the Debye-Callaway model considering Umklapp scattering.

Compound	**Approach**	$\mathbf{v}_l$ **(m/s)**	$\mathbf{v}_t$ **(m/s)**	**v (m/s)**	θ_D **(K)**	γ	κ_l **(Wm^{-1}K^{-1})**
TiNiSn	Slopes	6060.54	3358.89	3741.69	428.51	1.64	28.61
	`thermo_pw`	5672.68	3125.60	3467.67	397.13	1.47	29.04
	Ref.[3]	5426.00	3062.00	3406.00	392.00	1.58	29.00
ZrNiSn	Slopes	6021.41	3380.13	3761.50	417.54	1.60	34.61
	`thermo_pw`	5103.90	3069.61	3394.99	376.85	1.37	36.79
	Ref.[3]	5498.00	3149.00	3498.00	390.00	1.53	37.40
HfNiSn	Slopes	4900.15	2815.22	3126.77	348.65	1.51	29.85
	`thermo_pw`	4674.76	2752.94	3049.43	339.99	1.43	31.59
	Ref.[3]	4191.00	2503.00	2770.00	311.00	1.38	31.40

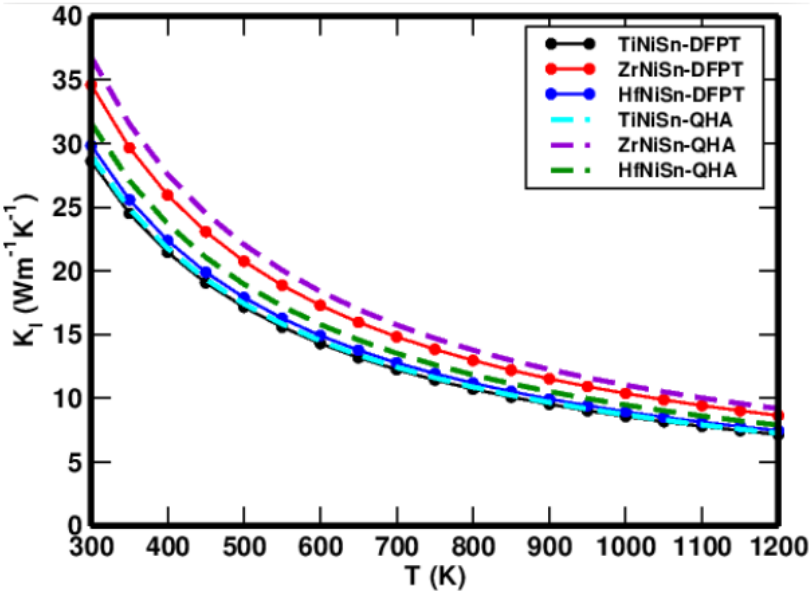

Figure 5: Variation of lattice thermal conductivity of XNiSn compounds with temperature using Slack's model with velocity determined from phonon bands by DFPT and QHA model in `thermo_pw` suite.

4 Conclusions and Concluding Remarks

The properties of XNiSn compounds, such as their structural, electronic, magnetic and phonon characteristics, are computed through DFT and DFPT. The calculated equilibrium lattice constants for TiNiSn, ZrNiSn and HfNiSn are 5.958Å, 6.154Å, 6.113Å respectively. Our study reveals that TiNiSn, ZrNiSn and HfNiSn are non magnetic semiconductors with indirect bandgap of 0.43 eV, 0.47 eV and 0.39 eV, respectively. The DoS near the Fermi level is mainly from 3d-Ni orbitals in VB and Ti, Zr, and Hf 's 3d/4d/5d orbitals, respectively in CB with Sn-5p orbitals having minor role in both bands. The phonon dispersion confirms the dynamic stability of the systems. The overlapping optical and acoustical phonon modes increase from TiNiSn to HfNiSn. The κ_l variation with temperature was assessed using Slack's model, with phonon velocity analyzed with QHA model and the slope of phonon bands by DFPT. The κ_l has observed to decrease as the temperature increases because of phonon scattering. The room temperature κ_l values of 28.61 Wm^{-1}K^{-1}, 34.61 Wm^{-1}K^{-1} and 29.85 Wm^{-1}K^{-1} for TiNiSn, ZrNiSn and HfNiSn respectively using DFPT follow same trend to those values 29.01 Wm^{-1}K^{-1}, 36.79 Wm^{-1}K^{-1} and 31.59 Wm^{-1}K^{-1} respectively by QHA model. The findings obtained through both approaches exhibit an agreement of 1.48%, 6.29%, and 5.82% for TiNiSn, ZrNiSn and HfNiSn, respectively. The values in present study are overestimated in comparison to prior methods. The scattering effects are to be included for matching the computational and ex-

perimental values for κ_l. Although the compounds have high κ_l at low temperatures, the decreasing values of them at elevated temperatures make them promising for high-temperature TE applications.

Acknowledgements

PK acknowledges the PhD grants award no. PhD-79/80-S&T-14 of UGC Nepal and NT-14 of ICTP/EAU for partial support. NPA acknowledges TU-NPAR-077/78 ERG14.

References

[1] G. J. Snyder and E. S. Toberer. Complex thermoelectric materials. *Nature Materials*, 7(2):105–114, 2008.

[2] H. J. Goldsmid. *Introduction to Thermoelectricity*, volume 121. Springer, 2016.

[3] R. J. Quinn and J. W. G. Bos. Advances in half-heusler alloys for thermoelectric power generation. *Materials Advances*, 2(19):6246–6266, 2021.

[4] G. D. Mahan and J. O. Sofo. The best thermoelectric. *Proceedings of the National Academy of Sciences*, 93(15):7436–7439, 1996.

[5] X. Zhang and L. D. Zhao. Thermoelectric materials: Energy conversion between heat and electricity. *Journal of Materiomics*, 1(2):92–105, 2015.

[6] Y. Pei, X. Shi, A. LaLonde, H. Wang, L. Chen, and G. J. Snyder. Convergence of electronic bands for high performance bulk thermoelectrics. *Nature*, 473(7345):66–69, 2011.

[7] Z. Feng, Y. Fu, Y. Zhang, and D. J. Singh. Characterization of rattling in relation to thermal conductivity: Ordered half-heusler semiconductors. *Physical Review B*, 101(6):064301, 2020.

[8] G. Ding, G. Y. Gao, and K. L. Yao. Examining the thermal conductivity of the half-heusler alloy tinisn by first-principles calculations. *Journal of Physics D: Applied Physics*, 48(23):235302, 2015.

[9] Y. Zhang. First-principles debye–callaway approach to lattice thermal conductivity. *Journal of Materiomics*, 2(3):237–247, 2016.

[10] J. S. Dugdale and D. K. C. MacDonald. Lattice thermal conductivity. *Physical Review*, 98(6):1751, 1955.

[11] H. Kim, G. Park, S. Park, and W. Kim. Strategies for manipulating phonon transport in solids. *ACS nano*, 15(2):2182–2196, 2021.

[12] P. Bagheri, P. Reddy, J. H. Kim, R. Rounds, T. Sochacki, R. Kirste, and Z. Sitar. Impact of impurity-based phonon resonant scattering on thermal conductivity of single crystalline gan. *Applied Physics Letters*, 117(8), 2020.

[13] W. Kim. Strategies for engineering phonon transport in thermoelectrics. *Journal of Materials Chemistry C*, 3(40):10336–10348, 2015.

[14] H. Xie, H. Wang, Y. Pei, C. Fu, X. Liu, G. J. Snyder, and T. Zhu. Beneficial contribution of alloy disorder to electron and phonon transport in half-heusler thermoelectric materials. *Advanced Functional Materials*, 23(41):5123–5130, 2013.

[15] S. H. Zaferani, R. Ghomashchi, and D. Vashaee. Strategies for engineering phonon transport in heusler thermoelectric compounds. *Renewable and Sustainable Energy Reviews*, 112:158–169, 2019.

[16] R. He, T. Zhu, Y. Wang, U. Wolff, J. C. Jaud, A. Sotnikov, and G. Schierning. Unveiling the phonon scattering mechanisms in half-heusler thermoelectric compounds. *Energy & Environmental Science*, 13(12):5165–5176, 2020.

[17] J. M. Ziman. *Electrons and Phonons: The Theory of Transport Phenomena in Solids*. Clarendon, Oxford, 1960.

[18] J. J. Gutiérrez Moreno, J. Cao, M. Fronzi, and M. H. N. Assadi. A review of recent progress in thermoelectric materials through computational methods. *Materials for Renewable and Sustainable Energy*, 9:1–22, 2020.

[19] W. Li, J. Carrete, N. A. Katcho, and N. Mingo. Shengbte: A solver of the boltzmann transport equation for phonons. *Computer Physics Communications*, 185(6):1747–1758, 2014.

[20] A. J. McGaughey and M. Kaviany. Phonon transport in molecular dynamics simulations: formulation and thermal conductivity prediction. *Advances in heat transfer*, 39:169–255, 2006.

[21] A. Petersen, S. Bhattacharya, T. M. Tritt, and S. J. Poon. Critical analysis of lattice thermal conductivity of half-heusler alloys using variations of callaway model. *Journal of Applied Physics*, 117(3), 2015.

[22] D. T. Morelli and G. A. Slack. High lattice thermal conductivity solids. *High thermal conductivity materials*, pages 37–68, 2006.

[23] R. Tranås, O. M. Løvvik, O. Tomic, and K. Berland. Lattice thermal conductivity of half-heuslers with density functional theory and machine learning: Enhancing predictivity by active sampling with principal component analysis. *Computational Materials Science*, 202:110938, 2022.

[24] S. N. H. Eliassen. A first principles study of lattice thermal conductivity in xnisn (x= ti, zr, hf) half-heusler alloys for thermoelectric applications, 2016.

[25] J. Carrete, W. Li, N. Mingo, S. Wang, and S. Curtarolo. Finding unprecedentedly low-thermal-conductivity half-heusler semiconductors via high-throughput materials modeling. *Physical Review X*, 4(1):011019, 2014.

[26] H. Muta, T. Yamaguchi, K. Kurosaki, and S. Yamanaka. Thermoelectric properties of zrnisn based half heusler compounds. In *ICT 2005. 24th International Conference on Thermoelectrics*, pages 351–354, 2005.

[27] Q. Shen, L. Zhang, L. Chen, T. Goto, and T. Hirai. Thermoelectric properties of zrnisn-based half-heusler compounds by solid state reaction method. *Journal of materials science letters*, 20(24):2197–2199, 2001.

[28] Y. Kimura and Y. W. Chai. Ordered structures and thermoelectric properties of mnisn (m= ti, zr, hf)-based half-heusler compounds affected by close relationship with heusler compounds. *Jom*, 67:233–245, 2015.

[29] P. O. Adebambo, B. I. Adetunji, O. T. Uto, S. Kenmoe, and G. A. Adebayo. First-principles calculations of the phonon, mechanical and thermoelectric properties of half-heusler alloy virsi alloys. *Crystals*, 12(12):1838, 2022.

[30] S. Baroni, S. De Gironcoli, A. Dal Corso, and P. Giannozzi. Phonons and related crystal properties from density-functional perturbation theory. *Reviews of modern Physics*, 73(2):515, 2001.

[31] P. Hohenberg and W. Kohn. Inhomogeneous electron gas. *Physical review*, 136(3B):B864, 1964.

[32] P. Giannozzi, S. Baroni, N. Bonini, M. Calandra, R. Car, C. Cavazzoni, and R. M. Wentzcovitch. Quantum espresso: a modular and open-source software project for quantum simulations of materials. *Journal of physics: Condensed matter*, 21(39):395502, 2009.

[33] J. P. Perdew, K. Burke, and M. Ernzerhof. Generalized gradient approximation made simple. *Physical review letters*, 77(18):3865, 1996.

[34] S. Grimme. Accurate description of van der waals complexes by density functional theory including empirical corrections. *Journal of computational chemistry*, 25(12):1463–1473, 2004.

[35] H. J. Monkhorst and J. D. Pack. Special points for brillouin-zone integrations. *Physical review B*, 13(12):5188, 1976.

[36] N. Marzari, D. Vanderbilt, A. De Vita, and M. C. Payne. Thermal contraction and disordering of the al (110) surface. *Physical Review Letters*, 82(16):3296, 1999.

[37] F. D. Murnaghan. The compressibility of media under extreme pressures. *Proceedings of the National Academy of Sciences*, 30(9):244–247, 1944.

[38] F. G. Aliev, N. B. Brandt, V. V. Moshchalkov, V. V. Kozyrkov, R. V. Skolozdra, and A. I. Belogorokhov. Gap at the fermi level in the intermetallic vacancy system rbisn (r= ti, zr, hf). *Zeitschrift für Physik B Condensed Matter*, 75:167–171, 1989.

[39] S. Öğüt and K. M. Rabe. Band gap and stability in the ternary intermetallic compounds nisnm (m= ti, zr, hf): A first-principles study. *Physical Review B*, 51(16):10443, 1995.

[40] J. Yang, H. Li, T. Wu, W. Zhang, L. Chen, and J. Yang. Evaluation of half-heusler compounds as thermoelectric materials based on the calculated electrical transport properties. *Advanced Functional Materials*, 18(19):2880–2888, 2008.

[41] D. F. Zou, S. H. Xie, Y. Y. Liu, J. G. Lin, and J. Y. Li. Electronic structure and thermoelectric properties of half-heusler zr0.5hf0.5nisn by first-principles calculations. *Journal of Applied Physics*, 113(19), 2013.

[42] J. Zhang, X. Zhang, and Y. Wang. Hf/sb co-doping induced high thermoelectric performance of zrnisn: First-principles calculation. *Scientific Reports*, 7(1):14590, 2017.

[43] W. Y. S. Lim, D. Zhang, S. S. F. Duran, X. Y. Tan, C. K. I. Tan, J. Xu, and A. Suwardi. A systematic approach for semiconductor half-heusler. *Frontiers in Materials*, 8:745698, 2021.

[44] A. J. Hong, L. Li, R. He, J. J. Gong, Z. B. Yan, K. F. Wang, and Z. F. Ren. Full-scale computation for all the thermoelectric property parameters of half-heusler compounds. *Scientific Reports*, 6(1):22778, 2016.

[45] G. A. Naydenov, P. J. Hasnip, V. K. Lazarov, and M. I. J. Probert. Huge power factor in p-type half-heusler alloys nbfesb and tafesb. *Journal of Physics: Materials*, 2(3):035002, 2019.

[46] N. Soga and O. L. Anderson. Simplified method for calculating elastic moduli of ceramic powder from compressibility and debye temperature data. *Journal of the American Ceramic Society*, 49(6):318–322, 1966.

[47] C. Malica and A. Dal Corso. Quasi-harmonic temperature dependent elastic constants: applications to silicon, aluminum, and silver. *Journal of Physics: Condensed Matter*, 32(31):315902, 2020.

[48] M. Schrade, K. Berland, S. N. Eliassen, M. N. Guzik, C. Echevarria-Bonet, M. H. Sørby, and T. G. Finstad. The role of grain boundary scattering in reducing the thermal conductivity of polycrystalline xnisn (x= hf, zr, ti) half-heusler alloys. *Scientific Reports*, 7(1):13760, 2017.

[49] G. Qin, A. Huang, Y. Liu, H. Wang, Z. Qin, X. Jiang, and M. Hu. High-throughput computational evaluation of lattice thermal conductivity using an optimized slack model. *Materials Advances*, 3(17):6826–6830, 2022.

[50] H. Ma, C. L. Yang, M. S. Wang, X. G. Ma, and Y. G. Yi. Effect of m elements (m= ti, zr, and hf) on thermoelectric performance of the half-heusler compounds mcobi. *Journal of Physics D: Applied Physics*, 52(25):255501, 2019.

[51] C. Toher, J. J. Plata, O. Levy, M. De Jong, M. Asta, M. B. Nardelli, and S. Curtarolo. High-throughput computational screening of thermal conductivity, debye temperature, and grüneisen parameter using a quasiharmonic debye model. *Physical Review B*, 90(17):174107, 2014.